On the relation between FORMOSAT-7/COSMIC-2 radio occultation scintillation S4 index and co-located electron density profiles in 2020

***Duann Y.[1,2], Chang L. C.[1,2], Chao C.-K.[1,2], Lin C.-Y. [1,2], Liu J.-Y.[1,2], Hsiao T.-Y.[3], Chen S.-P.[4]**

[1] Department of Space Science and Engineering, National Central University, Taoyuan City, Taiwan

[2] Center for Astronautical Physics and Engineering, National Central University, Taoyuan City, Taiwan

[3] Nuclear Science and Technology Development Center, National Tsing Hua University, Hsinchu City, Taiwan

[4] Department of Earth Sciences, National Cheng Kung University, Tainan City, Taiwan

Abstract

Six Low earth orbiting FORMOSAT-7/COSMIC-2 (F7/C2) satellites were launched into 24° inclination on June 25th 2019. The F7/C2 onboard payload: the primary Tri-GNSS (Global Positioning System—GPS, GALILEO, and GLObal NAvigation Satellite System—GLONASS) RO System (TGRS) offers a great opportunity of resolving ionospheric profiles during the 2020 solar minimum. The result of F7/C2 data sampling density with unfilled bins on a 30°-longitude and 1-hr local time (LT) grid of each month reveals that the unfilled percentage of the ionospheric scintillation profile with a maximum ($S_4\ max$) ≥ 0.125 in 2020 is lower than 30% within geomagnetic latitude $\pm 15°$N. This indicates a level of sampling sufficient to resolve the planetary scale distribution of S_4 at sub-harmonic time scales within the equatorial and tropical regions. A connection between $S_4\ max \geq 0.125$ and LT frame wave-2 tidal forcing is observed as in the numerical experiments by *Chang et al.* (2021). The altitudes of $S_4\ max$, the co-located (within a 30-minute time difference of and ~1° of longitude and latitude spatial difference) height of peak electron density in the F_2-layer (*hmF2*), and the co-located maximum gradient of electron density at the bottomside *F*-layer ($\nabla_Z N_e$) are compared within 18 – 06 LT in this study, to study the occurrences and growth rate of equatorial plasma bubbles (EPBs) caused by plasma uplift after sunset. The winter anomaly (WA) of the strong $S_4\ max$ (≥ 0.5) occurrence rate is significant in American-Atlantic-African, while an anomaly during boreal autumn of the highest $S_4\ max \geq 0.125$ occurrence rate in the Pacific of all seasons and sectors is found. The comparisons of different LT, seasons, and longitudinal sectors are analyzed and discussed in this study, to improve our understanding of the relation between S_4 and the generation mechanism of EPBs during solar minimum.

Keywords: FORMOSAT-7/COSMIC-2 (F7/C2), ionospheric scintillation amplitude index (S_4), the peak electron density in *F2*-layer (*hmF2*), equatorial plasma bubbles (EPBs), wave-2 tide.

1. Introduction

The importance of this study is to clarify and compare the roles of S_4 index, height of peak electron density in the F_2-layer (*hmF2*), and co-located maximum gradient of electron density at the bottomside *F*-layer ($(\nabla_z N_e)_{max}$) in the seasonal and longitudinal Equatorial plasma bubbles (EPBs) occurrence rate by analyzing FORMOSAT-7/COSMIC-2 (F7/C2) Radio Occultation (RO) data in 2020. The current six F7/C2 microsatellites orbiting at ~540 – 550 km with 24° inclination begins to collect RO data while it is still under the calibration/validation period of the mission (*Lien et al.*, 2021) and reached the designated mission orbits in February 2021. The F7/C2 mission has increased the number of GNSS-RO profiles within a geographic latitude region of $\pm 40°$N from ~3,000 profiles to ~8,000 per day

(*Schreiner et al.*, 2020; *Ruston and Healy.*, 2021). The on-board calculation of S_4 index (Eq.1) is performed at a 10-second cadence based on underlying 50 Hz (GPS) and 100 Hz (GLONASS) signal-to-noise ratio (SNR) data from the primary Tri-GNSS Radio-occultation System (TGRS) payload, the quantity P denotes the signal power proportional to the square of the voltage SNR (*Straus et al.*, 2020).

$$S_4 = \sqrt{\frac{\langle P^2 \rangle - \langle P \rangle^2}{\langle P \rangle}} \quad (1)$$

Studies of EPBs based on SNR of the dual-frequency signal and rate of the total electron content (TEC) index have been conducted for almost two score years (*Yeh and Liu*, 1982; *Ma et al.*, 2019). With an abundant data source of Global Positioning System (GPS) RO vertical electron density (N_e) profiles vertically integrated between 200 – 800 km altitude and S_4 observations at low latitudes derived from the F7/C2 RO experiment, the relation of EPBs and RO-N_e profile is capable to be investigated. The dark stripes of 135.6 nm emission observed by the Global-scale Observations of the Limb and Disk (GOLD) mission are found to be coincident with RO-S_4 $\geq$ 0.5; while the weaker RO-S_4 $\geq$ 0.125 are co-located to the seeding EPBs at the bottomside ionosphere (*Chen et al.*, 2021). Furthermore, the month-longitude variations of the EPB occurrence rate maxima during the solar minimum observed by The Defense Meteorological Satellite Program (DMSP) in 1994 – 1997 (*Gentil et al.* 2006), Communications/Navigation Outage Forecasting System (C/NOFS) in 2008 – 2010 (*Huang et al.*, 2014), and F7/C2 in 2019 – 2020 (*Chen et al.*, 2021) are found distributing along the days when the angle between the geomagnetic declination and the dusk terminator is equal to zero. On the other hand, the longitudinal and seasonal distributions of the *hmF2* observed by FORMOSAT-3/COSMIC (F3/C) during the growth phase of EPBs from 2008 – 2013 by *Chou et al.* (2020) indicate that the casual relationship of EPBs and the *hmF2* should be examined in more detail. Therefore, the $S_4\ max$ altitude varying with LT in each longitudinal sector and its relation with the co-located electron density profile structure is focused in this study.

In addition, the seasonal pattern of the S_4 and its potential relationship with the tidal forcing in the LT frame is included in the main interests as well. The wave-2 lower boundary forcing such as DE1, DW3, S0, and SW4 has been found as a potential source for the enhancement of field-line integrated Rayleigh-Taylor (R-T) growth rates over the Pacific region during boreal summer in the TIE-GCM numerical experiment performed by *Chang et al.* (2021). The equatorial and tropical S_4 wave analysis is performed along altitude in this research to investigate the wave impact to the development of EPBs during different seasons. Moreover, the winter anomaly (WA) is found as an ionospheric phenomenon as well, which is related to the F_2-layer that the ionization level at a certain location during winter is higher than during summer (*Azpilicueta and Nava*, 2021). The WA of S_4 is also compared in the four sectors: America ($-90°$E$\sim -30°$E), Atlantic-Africa ($-30°$E$\sim 60°$E), Indian ($60°$E$\sim 150°$E), and Pacific ($150°$E$\sim -90°$E) in this study.

2. Observations

This study focuses on the comparison of F7/C2 ionospheric S_4 and co-located N_e profile acquired within a time difference of 30 minutes and spatial difference of 110 km ($\sim 1°$ of longitude and latitude). The F7/C2 Ne profiles included in a Level-2 (L2) category (ionPrf) and ionospheric scintillation index (S_4) included in Level-1b (L1b) categories (scn1c2 and podTc2) are provided by COSMIC Data Analysis and Archive Center (CDAAC, https://cdaac-www.cosmic.ucar.edu/cdaac/) and Taiwan Analysis Center for COSMIC (TACC, https://tacc.cwb.gov.tw/v2/) datasets (*Chen et al.*, 2021). The sampling density of N_e profiles and $S_4\ max \geq 0.125$ is illustrated in Figure 1, which shows the number of unfilled bins on a $30°$ longitude and 4-hr, 2-hr, 1-hr local time grid of each month from top to bottom at each latitude.

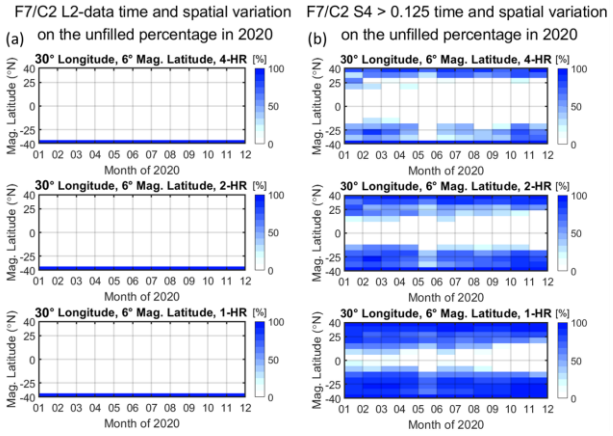

Figure 1. Percent of unfilled bins in grid of $30°$ longitude and $6°$ MLAT for F7/C2 (a) L2 (b) $S_4\ max > 0.125$ data, illustrating F7/C2 sampling density.

It can be seen in Figure 1 that from geomagnetic latitude (MLAT) $40°$N to $\sim 37°$S, full longitude/UT sampling of N_e data is available during most of 1-hr period. In addition, the sampling resolution of $S_4\ max \geq 0.125$ with binned longitude $30°$ and 1-hr, the coverage within $\pm 20°$N is adequate. Based on the sampling density result in Figure 1, the comparison of the geographic and altitudinal distributions of maximum S_4 ($S_4\ max$) density and co-located Ne profile is then shown in Figure 2 as an illustration for further analysis, and boreal winter is selected as an example here.

In the Figure 2 (a), a cluster of $S_4\ max \geq 0.5$ is concentrated within the region of Atlantic-America during boreal winter notably, scattering along the MLAT ±15°N. Furthermore, the density of $S_4\ max$ within $0°\sim 25°$N is higher than $0°\sim 25°$S during boreal winter (Figure 2 (b)), which is expected as a consequence of the WA. Figure 2 (c) illustrates all Ne profiles co-locating with the $S_4\ max$,

and the correlations between co-located $S_4\,max$, *hmF2* and $(\nabla_z N_e)_{max}$ in different seasons and longitudinal sectors are compared in the forthcoming sections.

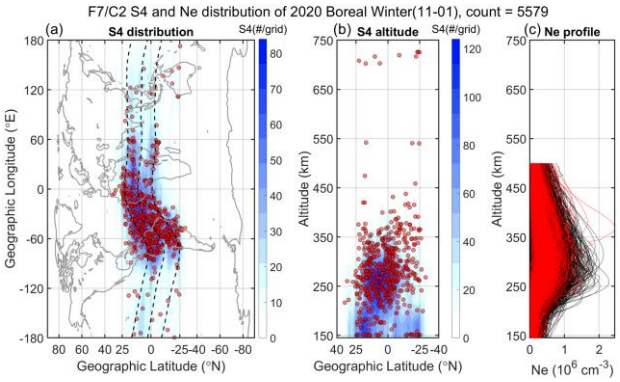

Figure 2. The F7/C2 $S_4\,max$ and Ne data distribution in geographic longitude (°S), latitude (°N) and altitude (km) in boreal winter 11-01 of 2020. The contour illustrates the density of $S_4\,max \geq 0.125$ of each binned grid that latitude 2.5°, longitude 30°, and altitude 50 km. $S_4\,max \geq 0.5$ are indicated as red spots. The black dashed lines denote the magnetic latitude (MLAT) 0° and ±15°. The three panels in each season are $S_4\,max$ geographic distribution (left), $S_4\,max$ latitude-altitude distribution (middle), and all Ne profiles (right), red lines indicated Ne profiles corresponding to $S_4\,max \geq 0.5$.

3. Results

The annual variation of the four longitude regions are analyzed as an overview of the correlations between each co-located factor. Figure 3 illustrates the time variation of $log_{10}((\nabla_z N_e)_{max})$ in 2020 as density plots, and compare $log_{10}((\nabla_z N_e)_{max})$ with the $S_4\,max \geq 0.5$ in the American sector as an example here.

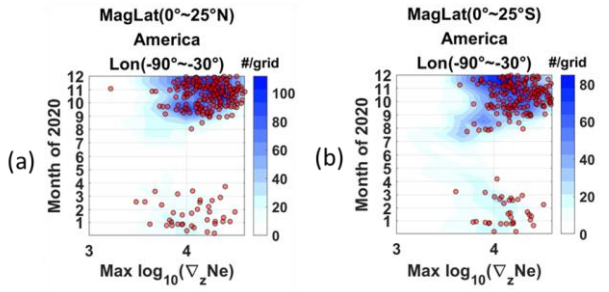

Figure 3. The time variation of F7/C2 $log_{10}((\nabla_z N_e)_{max})$ of each profile corresponding to RO-$S_4 \geq 0.125$ in 2020 for the sectors of America within MLAT (a) 0° to 25°N and (b) 0° to 25°S. $S_4 \geq 0.5$ are indicated as red spots. The contour illustrates the density of $S_4 \geq 0.125$ with grid of 30-day and 0.1-$log_{10}(\nabla N_e)$.

Notably, strong $S_4\,max$ (≥ 0.5) tends to be correlated with high $log_{10}((\nabla_z N_e)_{max})$ in Figure 3. In particular, the most concentrated cluster of strong $S_4\,max$ is found within the American sector. To investigate how the altitude of $S_4\,max$ occurrence varies in LT within different sectors and seasons, the LT-altitude variation of F7/C2 $S_4\,max$ within 16 – 08 LT is therefore analyzed in Figure 4.

The relative probability-LT for all EPBs seen in each longitude sector and each year from August 2008 to December 2014 has been compared by *Smith and Heelis* (2017). The results in 2009 – 2010 solar minimum show that EPBs in the Pacific sector extend most effectively toward dawn. In Figure 4, the sectors of America and Pacific are selected here to show different patterns of seasonal anomaly in LT-altitude variations.

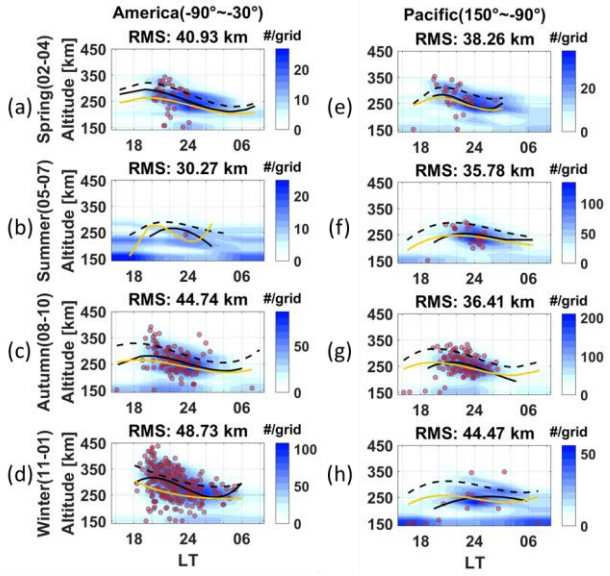

Figure 4. The LT-altitude variation of F7/C2 $S_4\,max$ within 16 – 08 LT in boreal seasons of 2020 for the American and Pacific sectors within MLAT ±25°. The black line in each subplot denotes the 3rd degree polynomial fitting of $S_4\,max \geq 0.25$ with root mean square (RMS). The yellow line is $(\nabla_z N_e)_{max}$ altitude wherein $S_4\,max \geq 0.25$, and black dashed line is *hmF2* wherein $S_4\,max \geq 0.25$. The contour illustrates the density of $S_4\,max \geq 0.125$ with grid of 2-hour and 20-km. $S_4 \geq 0.5$ are indicated as red spots.

Subsequently, the analysis indicates that the seeding EPB occurrence rate related to $S_4\,max \geq 0.125$ is lower during boreal summer, especially in the American (Figure 4 (b)) and Indian (not shown here) sectors, which coincides with the similar results of TIE-GCM wave-2 tidal forcing numerical experiments by *Chang et al.* (2021). Additionally, an autumn anomaly $S_4\,max \geq 0.125$ in the Pacific (Figure 4 (g)) is observed as the highest occurrence of all, with strong $S_4\,max$ constrained < 350 km and less than American winter (Figure 4 (d)). On the other hand, the altitude of $S_4\,max$ commonly decays during post-midnight and the cluster of strong $S_4\,max$ within *F*-layer last after 03 LT is only in the case that the altitude difference of $(\nabla_z N_e)_{max}$ and $S_4\,max \geq 0.25$ enlarges increasingly (the altitude of $S_4\,max \geq 0.25$ ascends) after 02 LT, such as the America sector in boreal winter (Figure 4 (d)). Ultimately, the relation of the altitude of $(\nabla_z N_e)_{max}$ and $S_4\,max \geq 0.25$ is an essential factor to study this seasonal diversity along geographic longitudes, and the correlation between *hmF2*, $(\nabla_z N_e)_{max}$, and $S_4\,max$ with different scales of $S_4\,max$ will be discussed later.

Afterwards, the ionospheric wave analysis is applied to see the wave components that related to the vertical distribution of $S_4\,max$ within the equatorial (MLAT ±5°N) and tropical regions (MLAT $\pm5\sim\pm15$°N) (Figure 5). The terdiurnal wave analysis of tropical regions are especially illustrated here as a highlight, and the positive/negative zonal wavenumbers in the x-axis represent the eastward/westward propagating tides.

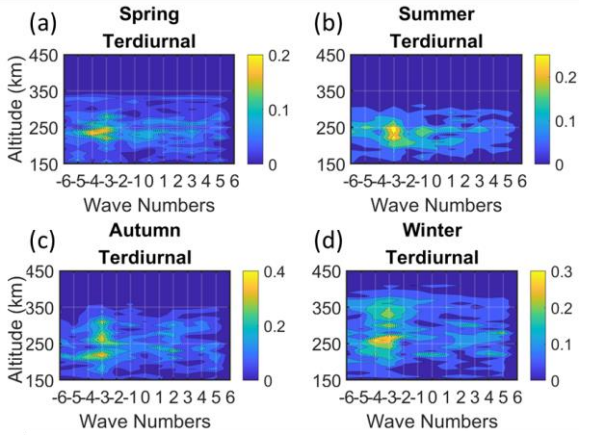

Figure 5. The terdiurnal altitudinal wave amplitude of F7/C2 $S_4\,max \geq$ 0.125 amount within equatorial region (MLAT ±5°N) in boreal seasons of 2020.

Although the diurnal and semidiurnal tides are not shown in Figure 5, the migrating tides DW1, SW2, and TW3 are dominants components in both equatorial (not shown here) and tropical regions during every boreal season, especially at the altitude of ~ 250 km. Furthermore, there are secondary peaks of non-migrating tides DE1, S0, and TW1 during boreal summer in both equatorial and tropical regions. Nevertheless, there is a discontinuity of altitudinal expansion in tropical TW3 can be noticed that the main peak at ~250 km and two weaker peaks above at ~300 km and ~ 330 km during boreal winter (Figure 5 (d)), while this breaking exists as well during boreal autumn, but the peaks are shifted lower to the altitude of ~200 km, ~250 km, and ~ 300 km (Figure 5 (c)). TW3 in the middle atmosphere is allowed to propagate to higher altitudes due to very long vertical wavelengths (*Chang et al.*, 2013; *Smith*, 2000; *Du and Ward*, 2010; *Venkateswara Rao et al.*, 2011), and the ionospheric TW3 response at below 300 km is partially contributed from the neutral atmospheric TW3 and the SW2 tide forced from below, while there are still other unknown interacting sources (*Pancheva et al.*, 2012) that may contribute to TW3 discontinuity in $S_4\,max$ altitude during boreal autumn and winter of solar minimum.

4. Discussions and Conclusions

Analysis of FORMOSAT-7/COSMIC-2 observed $(\nabla_z N_e)_{max}$, $S_4\,max$, and *hmF2* in 2020 was performed to understand the seasonal, zonal, temporal variations of low-latitude ionosphere *F*-region in different longitude sectors during solar minimum, and the correlations between these physical parameters and EPBs occurrence.

The correlation of the altitude of F7/C2 $(\nabla_z N_e)_{max}$ and $S_4\,max$ within MLAT $25°\text{N}-25°\text{S}$ is demonstrated in Figure 6. Noted that the correlations between *hmF2* and $S_4\,max$, and between *hmF2* and $(\nabla_z N_e)_{max}$ are analyzed as well in this research but not shown as figures here.

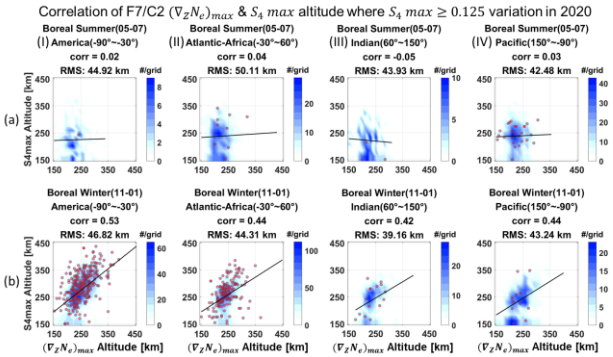

Figure 6. The correlation of F7/C2 $log_{10}((\nabla_z N_e)_{max})$ and $S_4\,max$ altitude of each profile corresponding to $S_4 \geq 0.125$ within MLAT $25°\text{N}-25°\text{S}$ and different sectors of (I) American, (II) Atlantic-Africa, (III) Indian, and (IV) Pacific in boreal (a) summer and (b) winter of 2020. The contour illustrates the density of $S_4 \geq 0.125$ with grid of 20-km. $S_4 \geq 0.5$ are indicated as red spots.

In Figure 6, the boreal winter-summer difference of the correlations is magnificent. Namely, the altitude of $S_4\,max$ occurrence is much more related to the altitude of $(\nabla_z N_e)_{max}$ during boreal winter than during boreal summer, but this feature is independent of the $S_4\,max$ occurrence rate, according to the fact that the grid density of $S_4\,max$ in the Pacific sector during boreal summer (Figure 6 (a-IV)) is larger than boreal winter (Figure 6 (b-IV)). Ultimately, the correlations with 95% confidence interval in Figures 6 corresponding to different scales of $S_4\,max$ are compared in Figure 7.

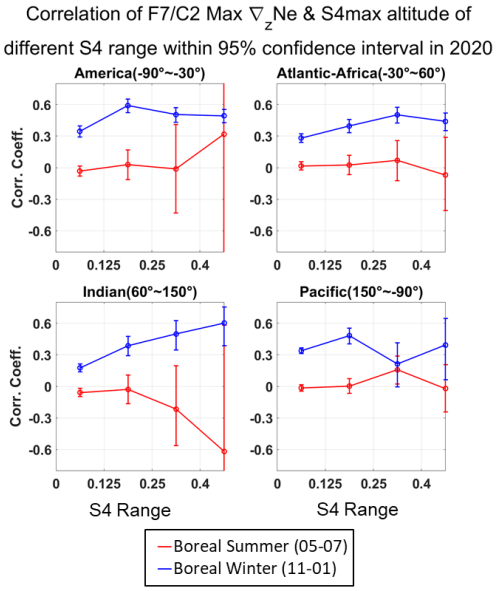

Figure 7. The correlation with 95% confidence interval of F7/C2 $(\nabla_z N_e)_{max}$ and $S_4\,max$ altitude within low latitude region corresponding to different range of S_4 in boreal summer (red line) and winter (Blue line) of 2020.

The correlation between $S_4\,max$ and either $(\nabla_z N_e)_{max}$ (Figure 7) or *hmF2* (not shown here) generally increases with the enhancement of $S_4\,max$ during boreal winter, and decreases with the enhancement of $S_4\,max$ during boreal summer, this winter-summer pattern is especially significant in the Indian sector, but only except for the American sector. In Figure 7, the boreal winter correlation variation in the American sector almost remains constant when $S_4\,max \geq 0.125$, but the boreal summer correlation grows when the corresponding $S_4\,max$ scale level increases. To sum up, the altitude of $S_4\,max$ is partially correlated (~0.5) with $(\nabla_z N_e)_{max}$ during boreal winter, but not correlated (~0) during boreal summer. Moreover, the variation of the correlations between the altitude of $S_4\,max$ and *hmF2* along the $S_4\,max$ scale level presents a trend almost the same as the correlations between the altitude of $S_4\,max$ and $(\nabla_z N_e)_{max}$.

Consequently, it can be highlighted that a boreal autumn anomaly of $S_4\,max \geq 0.125$ in the Pacific sector is observed as the highest occurrence of all sectors and seasons in 2020. Furthermore, the sub-harmonic wave analysis in this study reveals that the signal of wave-2 components (DE1, DW3, S0, SW4, TW1, and TW5) is found to be strong during boreal summer in 2020, and an altitudinal discontinuity of TW3 exists during boreal autumn and winter can be noticed in the tropical region. On the other hand, the correlations between *hmF2* and the altitude of $(\nabla_z N_e)_{max}$ during boreal summer (winter) increase (decrease) when the $S_4\,max$ scale level is raised (not shown in the figures). While the $S_4\,max \geq 0.25$ has an increasing inverse correlation during boreal summer with the altitudes of $(\nabla_z N_e)_{max}$ and *hmF2* in the Indian sector, but this feature is opposite to the American sector.

References

Azpilicueta, F. and B. Nava (2021), A different view of the ionospheric winter anomaly, *Adv. Space Res.*, 67(1):150-162, doi: 10.1016/j.asr.2020.10.039.

Chang, L. C., C.-H. Lin, J.-Y. Liu, N. Balan, J. Yue, and J.-T. Lin (2013), Seasonal and local time variation of ionospheric migrating tides in 2007–2011 FORMOSAT-3/COSMIC and TIE-GCM total electron content, *J. Geophys. Res., Space Physics*, 118:2545–2564, doi:10.1002/jgra.50268.

Chang, L. C., C. C. J. H. Salinas, Y. -C. Chiu, M. Jr. Jones, P. K. Rajesh, C.-K. Chao, J. -Y. Liu, C. C. H. Lin, and T. -Y. Hsiao (2021), Implication of tidal forcing effects on the zonal variation of solstice equatorial plasma bubbles, *J. Geophys. Res., Space Physics*, 126, e2020JA028295, doi: 10.1029/2020JA028295.

Chou, M.-Y., Q. Wu, N. M. Pedatella, I. Cherniak, W. S. Schreiner, and J. Braun (2020), Climatology of the Equatorial Plasma Bubbles Captured by FORMOSAT-3/COSMIC, *J. Geophys. Res., Space Physics*, 125(5), doi: 10.1029/2019JA027680.

Du, J., and W. E. Ward (2010), Terdiurnal tide in the extended Canadian Middle Atmospheric Model (CMAM), *J. Geophys. Res.*, 115, D24106, doi: 10.1029/2010JD014479.

Gentile, L. C., W. J. Burke, and F. J. Rich (2006), A global climatology for equatorial plasma bubbles in the topside ionosphere, *Ann. Geophys.*, 24:163–172, doi: 10.5194/angeo-24-163-2006.

Huang, C.-S., O. de La Beaujardiere, P. A. Roddy, D. E. Hunton, J.-Y. Liu, and S. -P. Chen (2014), Occurrence probability and amplitude of equatorial ionospheric irregularities associated with plasma bubbles during low and moderate solar activities (2008–2012), *J. Geophys. Res., Space Physics*, 119:1186–1199, doi: 10.1002/2013JA019212.

Lien, G. -Y., C. -H. Lin, Z. -M. Huang, W. -H. Teng, J. -H. Chen, C. -C. Lin, H. -H. Ho, J. -Y. Huang, J. -S. Hong, C. -P. Cheng, C. -Y. Huang (2021), Assimilation Impact of Early FORMOSAT-7/COSMIC-2 GNSS Radio Occultation Data with Taiwan's CWB Global Forecast System, *Mon. Weather Rev.* (published online ahead of print 2021), doi: 10.1175/MWR-D-20-0267.1.

Ma, G., K. Hocke, J. Li, Q. Wan, W. Lu, W. Fu (2019), GNSS Ionosphere Sounding of Equatorial Plasma Bubbles, *Atmosphere*, 10(11):676, doi: 10.3390/atmos10110676.

Pancheva, D., Y. Miyoshi, P. Mukhtarov, H. Jin, H. Shinagawa, and H. Fujiwara (2012), Global response of the ionosphere to atmospheric tides forced from below: Comparison between COSMIC measurements and simulations by atmosphere-ionosphere coupled model GAIA, *J. Geophys. Res.*, 117, A07319, doi: 10.1029/2011JA017452.

Ruston, B. and S. Healy (2021), Forecast Impact of FORMOSAT-7/COSMIC-2 GNSS Radio Occultation Measurements, *Atmos. Sci. Lett.*, 22:e1019, doi: 10.1002/asl.1019.

Schreiner, W. S., J. P. Weiss, R. A. Anthes, J. Braun, V. Chu, J. Fong, D. Hunt, Y. H. Kuo, T. Meehan, W. Serafino, J. Sjoberg, S. Sokolovskiy, E. Talaat, T. K. Wee, and Z. Zeng (2020), COSMIC-2 radio occultation constellation: First results, *Geophys. Res. Lett.*, 47, e2019GL086841, doi: 10.1029/2019GL086841.

Smith, A. K. (2000), Structure of the terdiurnal tide at 95 km, *Geophys. Res. Lett.*, 27(2): 177–180, doi:10.1029/1999GL010843.

Smith, J., and R. A. Heelis (2017), Equatorial plasma bubbles: Variations of occurrence and spatial scale in local time, longitude, season, and solar activity, *J. Geophys. Res., Space Physics*, 122:5743–5755, doi:10.1002/2017JA024128.

Straus, P., W. Schreiner, J. Santiago, E. Talaat, C. -L. Lin (2020), FORMOSAT-7/COSMIC-2 TGRS Space Weather Provisional Data Release 1, March 2020, 4–7.

Venkateswara Rao, N., T. Tsuda, S. Gurubaran, Y. Miyoshi, and H. Fujiwara (2011), On the occurrence and variability of the terdiurnal tide in the equatorial mesosphere and lower thermosphere and a comparison with the Kyushu-GCM, *J. Geophys. Res.*, 116, D02117, doi: 10.1029/2010JD014529.

Yeh, K. -C. and C. -H Liu (1982), Radio wave scintillations in the ionosphere, *Proc. IEEE*, 70(4):324-360, doi: 10.1109/PROC.1982.12313.